Chimeric identities and reduced stiffness characterise the shoot apex of *Arabidopsis* stem cell mutants

Running title: Properties of stem cell mutants

Léa Rambaud-Lavigne[1,*], Aritra Chatterjee[2,6], Simone Bovio[1,3], Virginie Battu[1], Quentin Lavigne[4], Namrata Gundiah[5,*], Arezki Boudaoud[1,7,*], Pradeep Das[1,*]

[1]Laboratoire Reproduction et Développement des Plantes, Université de Lyon, ENS de Lyon, UCB Lyon 1, CNRS, INRAE, INRIA, Lyon, France. [2]Centre for BioSystems Science and Engineering, Indian Institute of Science, Bengaluru, India. [3]PLATIM-LyMIC, Université de Lyon, ENS de Lyon, Inserm, CNRS, SFR Biosciences US8 UAR3444, UCB Lyon 1, Lyon, France. [4]Physikalisches Institut, Rheinische Friedrich-Wilhelms-Universität, 53115 Bonn, Germany. [5]Department of Mechanical Engineering, Indian Institute of Science, Bengaluru, India.

Present address: [6]Weldon School of Biomedical Engineering, Purdue University, West Lafayette, Indiana, USA. [7]LadHyX, CNRS, Ecole Polytechnique, Institut Polytechnique de Paris, 91128 Palaiseau Cedex, France

[*]Authors for correspondence (lea.rambaud1@ens-lyon.fr, namrata@iisc.ac.in, arezki.boudaoud@polytechnique.edu, pradeep.das@ens-lyon.fr)

ORCID: LRL, 0000-0001-6560-5359; AC, 0000-0002-5318-3459; SB, 0000-0002-9836-6742; VB, 0009-0009-1098-4633; QL, 0000-0003-2326-2604; NG, 0000-0002-9882-5232; AB, 0000-0002-2780-4717; PD, 0000-0002-1179-9044

Key words: shoot apical meristem, *WUSCHEL*, *CLAVATA*, heterogeneities, morphogenesis, stem cell mechanics

Summary statement: Mechanical, genetic and functional evidence supported by theoretical models call into question the current definition of stem cells in the shoot apex.

Abstract

Stem cell homeostasis in the shoot apical meristem involves a core regulatory feedback loop between the signalling peptide CLAVATA3, produced in stem cells, and the transcription factor WUSCHEL, expressed in the underlying organising centre. Compromised CLAVATA activity leads to massive meristem overgrowth, which is thought to be caused by stem cell overproliferation. However, it is unknown how uncontrolled stem cell divisions lead to the specific changes observed in *clavata* mutants. Here we first quantitatively characterise these mutants, to reveal underlying tissue curvature defects. We use analytical models to show how perturbed mechanical properties and/or growth rates may contribute to altered meristem morphology. Indeed, we find that *clavata* meristems are softer than the wild type, and that stereotypical meristem organisation is lost, with cells instead simultaneously expressing multiple domain markers. Furthermore, we show that mutant meristematic cells are auxin-responsive, suggesting that they are functionally different from wild-type stem cells. We propose that the *clavata* phenotype is not caused by stem cell overproliferation, but rather by the disruption of a more complex regulatory framework that is key to maintaining distinct genetic and functional domains at the shoot apex.

Introduction

The shoot apical meristem (SAM) is a structure at the growing tip of the plant that gives rise to all its aboveground tissues. The SAM is sustained by the activity of a small pool of centrally-located undifferentiated stem cells in the slow-dividing central zone (CZ). Through successive divisions, their daughter cells exit from the CZ into the surrounding peripheral zone (PZ), where they may differentiate into lateral organs, such as leaves or flowers. The CZ is itself maintained via the activity of the underlying organising centre (OC) (Laux et al., 1996).

The regulatory network driving stem cell maintenance in *Arabidopsis* is well studied. At its core is a feedback loop between WUSCHEL (WUS), a homeobox transcription factor expressed in the OC, and CLAVATA3 (CLV3), a signalling peptide expressed in the CZ (Brand et al., 2000; Clark et al., 1995; Laux et al., 1996; Schoof et al., 2000). The movement of WUS from the OC to the CZ is necessary for inducing stem cell identity, by directly binding to the *CLV3* promoter and activating its expression (Daum et al., 2014; Yadav et al., 2011). In turn, CLV3 binds receptors such as the leucine-rich-repeat receptor-like kinase CLV1 (Clark et al., 1997), and the receptor-like proteins CLV2 (Kayes and Clark, 1998) and CORYNE (CRN) (Fletcher et al., 1999; Jeong et al., 1999; Miwa et al., 2008; Müller et al., 2008). Signalling from these ligand-receptor complexes ultimately leads to the downregulation of *WUS* in the OC (Miwa et al., 2008; Müller et al., 2006). The absence of WUS activity leads to SAM arrest early in development (Laux et al., 1996), whereas the loss of the *CLV* genes leads to a vast enlargement of the SAM (Clark et al., 1993; Clark et al., 1995; Kayes and Clark, 1998), a phenomenon called fasciation. Several instances of fasciated tissues have been observed in the wild, as well as in crop plants, including beef tomatoes and the maize *fasciated ear2* (*fea2*) mutant (Taguchi-Shiobara, 2001). It is thought that fasciation is caused by stem cell overproliferation in the CZ (Brand et al., 2000; Busch et al., 2010; Dao et al., 2022; Kwon et al., 2005; Lenhard and Laux, 2003; Ma et al., 2019; Müller et al., 2008; Nimchuk et al., 2011; Whitewoods et al., 2018; Wu et al., 2005), or conceivably, by lower rates of cell transit from the CZ to the PZ (Laufs et al., 1998).

Over the years, *CLV3* has been the only known genetic marker to study stem cells at the shoot apex (Müller et al., 2006; Reddy and Meyerowitz, 2005), including for analysing *clv* mutants. While microarray analyses have uncovered several other genes that are enriched in the CZ (Aggarwal et al., 2010; Busch et al., 2010; Yadav et al., 2009), none have been extensively characterised. More recently, atomic force microscopy (AFM) experiments,

which measure cellular mechanical properties, revealed that *CLV3*-expressing cells are stiffer than surrounding PZ cells, and that in flowers, the onset of *CLV3* expression coincides with an increase in cell wall stiffness (Milani et al., 2014). Thus, although stem cell identity is both spatially and temporally associated with increased cell stiffness (Milani et al., 2014), it is unknown how these mechanical patterns are altered when stem cell regulation is perturbed.

The core stem cell regulatory network is also influenced by hormone signalling, including cytokinin and auxin (Gordon et al., 2009; Busch et al., 2010). Exogenous cytokinin treatment phenocopies the *clv* mutant by increasing *WUS* expression and decreasing *CLV1* expression (Lindsay et al., 2006). While exogenous auxin treatment induces organogenesis markers in the PZ, the CZ itself remains unaffected, displaying reduced responsivity to auxin (de Reuille et al., 2006). Whereas in the PZ, the auxin response factor MONOPTEROS (MP) activates the expression of lateral organ identity genes in an auxin-dependent manner (Berleth and Jürgens, 1993; Bhatia et al., 2016; Hardtke and Berleth, 1998; Yamaguchi et al., 2013), it also functions to repress CZ genes that are themselves activators of *CLV3* expression (Luo et al., 2018; Zhao et al., 2010). Despite these advances, it remains unclear how auxin signalling is perturbed in *clv* mutants, and furthermore, whether this plays a direct role in generating the fasciated *clv* phenotype.

In this study, we use quantitative approaches to study the effects of the loss of proper stem cell regulation that reveal hitherto unobserved cellular and tissular phenotypes, such as cell size and local surface curvature in *clv* mutant SAM. We run analytical mechanical models to show that differences in stiffness and/or growth regimes are sufficient to account for the surface curvature defects observed in *clv* mutants. We examine the mechanical properties and genetic identities of *clv* mutant SAM to provide experimental support for these model predictions. Lastly, we show that these differences are correlated with altered sensitivity to auxin.

Results

Altered cellular and tissular properties characterise fasciated *clv* SAM

In order to better understand the defects associated with abnormal stem cell regulation, we first quantified the highly fasciated phenotype of the canonical *clv3-2* allele (Clark et al., 1995). In our growth conditions, shoot meristems in WT plants consistently display a

87 stereotypical dome shape, whereas *clv3-2* meristems display a highly variable phenotype,
88 most often comprising a large centrally-located bulge from which two or more arm-like
89 outgrowths elongate laterally (Fig. 1A, B). A more detailed analysis using scanning electron
90 microscopy (SEM) reveals that the cellular organisation also varies between the central
91 bulge, which is usually devoid of any discernible organisation, and the lateral arms, which
92 are mostly composed of cell files (Fig. 1C, D). Both the central bulge and the lateral
93 elongations give each SAM a unique aspect, with irregular shapes for the bulge and varying
94 numbers and shapes for the arms (Fig. 1E-G, Fig. S1A).
95
96 Previous studies had suggested that cell size in *clv* mutant SAM differs from the WT (Laufs
97 et al., 1998; Schoof et al., 2000). We wondered whether we could use such changes in
98 cellular morphologies to further characterise the mutant phenotypes described above. To
99 quantify cell size, we acquired 3D image stacks of SAM from WT as well as from multiple
100 *clv1* and *clv3* mutant lines. Using only cells at the uppermost regions of the SAM within the
101 image stack, we next extracted slices near the midpoint of cells in the L1 and L2 layers,
102 segmented them using the MorphoGraphX software (Barbier de Reuille et al., 2015) and
103 determined cell areas. We found that across 3 WT SAM, the average cell size is similar in
104 both cell layers, with L1 cells at 23.9 ± 5.83 μm^2 (n = 103) and L2 cells at 24.5 ± 7.18 μm^2
105 (n = 115) (Fig. 1H). In contrast, L2 cells in *clv3-2* mutants are on average 69% larger than
106 L1 cells – 31.2 $\pm$ 9.84 μm^2 in the L2 versus 18.4 $\pm$ 5.34 μm^2 in the L1 (Fig. 1H). A similar
107 trend was observed for other *clv* alleles, such as *clv1-8* and *clv3-7*, suggesting that altered
108 morphology is a general feature of *clv* mutants. (Fig. S1B).
109
110 In order to ensure that the observed changes in cell areas were not imaging artefacts, we
111 next measured cell volumes in WT and *clv3-2* SAM. To this end, we generated 3D
112 reconstructions using the MARS pipeline (Fernandez et al., 2010), which involves acquiring
113 images of samples from multiple angles and fusing them to generate high-resolution images
114 that are then segmented. Consistent with our findings for cell areas, we found that while L1
115 and L2 cells have similar volumes in the WT (136.51 $\pm$ 40.45 μm^3 and 148.72 $\pm$ 44.54 μm^3,
116 respectively), L2 cells in *clv3-2* SAM are almost twice as large as L1 cells (249.08 $\pm$ 130.65
117 μm^3 vs 129.48 $\pm$ 40.86 μm^3) (Fig. 1I and Fig. S1C).
118
119 An examination of the SEM and confocal images had suggested that meristems in *clv3*
120 mutants are less smooth than WT meristems. One way to better study this is by measuring
121 curvature. To this end, we used a method (Kiss et al., 2017) to precisely detect the outer

surface of the SAM in our high-resolution 3D MARS-reconstructed image stacks, and calculated Gaussian curvature within a 10-μm radius at every pixel of that surface in WT and mutant SAM. We observe stereotypical patterns of local curvature in WT inflorescences, with the SAM and young flowers being homogeneously smooth areas that are separated by boundaries defined by negative curvature (Fig. 1J). In contrast, even the uppermost areas of *clv3-2* SAM, which are distant from the regions where flowers form, display a much more variable surface curvature, with crests and troughs of various sizes distributed throughout the SAM (Fig. 1K). These findings suggest that the arrangement of local curvature that typifies WT meristems is lost in *clv3-2* mutants.

Morphoelastic models reveal how growth and stiffness contribute to surface buckling

To elucidate a theoretical basis for the surface curvature defects of *clv* mutants, we next generated analytical models of SAM development using a growth and remodelling framework (Goriely, 2017). Specifically, we adapted a model developed to explore the biomechanical basis of morphogenesis in systems that display buckling behaviours similar to that observed in *clv* mutants (Almet et al., 2019; Moulton et al., 2013). We modelled the SAM as an axially growing planar elastic rod (the outer L1 layer), attached to an elastic foundation (the inner layers), and clamped at the two ends (Fig. S2). We used the theoretical model to explore how growth stretch, a proxy for tissue growth, and/or mechanical properties, a proxy for cellular stiffness, might contribute to the altered morphology of *clv* mutants (see Supplementary Materials and Methods).

First, we used linear stability analysis to plot output shapes when either only growth stretch (γ) or system stiffness ($\hat{k}$, where *k* is the ratio of foundation and rod stiffnesses) was varied. When the foundation and rod had similar mechanical properties ($\hat{k}$ = 1) and when growth stretch was at a low, subcritical value (γ^*_{inf}= 5.82), the output shape resembled the smooth dome of a WT meristem (Fig. 2A). When growth stretch was raised to a near-critical point (γ^*_{inf}= 8.99), the size of the dome increased, while remaining smooth. A further increase in growth stretch generated various modes of buckling (Fig. 2A) that broadly capture the surface curvature defects of *clv* mutants. Next, we investigated the role of system stiffness ($\hat{k}$) on SAM morphology, while maintaining a background of constant growth stretch (γ^* = 8.99) (Fig. 2B). No buckling was evident for higher values of $\hat{k}$ ($\hat{k}$>1), but when the stiffness was reduced ($\hat{k}$ = 0.5), we observed the appearance of buckling in the rod (Fig. 2B), similar to those obtained using growth values above the critical point (Fig. 2A). Together, these

156 analytical results indicate that in a biological context, cellular growth and stiffness
157 characteristics could influence tissue architecture of the SAM.
158
159 In contrast to the analytical shapes obtained above, *clv* mutant SAM in fact display highly
160 variable local buckling, such that the positions, numbers and amplitudes of folds differ within,
161 and between, individual mutant meristems. We reasoned that such variability could result
162 from heterogeneities in cellular characteristics that generate local differences in growth,
163 stiffness or both. To investigate the effects of local heterogeneities on buckling, we replaced
164 constant growth stretch or system stiffness with one of three distinct functions to generate
165 differential distributions across the rod (Fig. 2C). Indeed, all three functions generate
166 differential buckling over the length of the rod when either growth stretch (Fig. 2D, Fig. S3B-
167 B') or system stiffness (Fig. 2E) is spatially distributed, with the resulting shapes often closely
168 resembling the asymmetry and variable buckling amplitudes visible in sections through
169 various *clv* SAM in the literature. These results suggest that local differences in growth or
170 stiffness within the SAM could explain the phenotypes of *clv* mutants.
171
172 Finally, we asked whether variations in system stiffness and growth stretch could act
173 together to generate even greater differences in buckling characteristics. To this end, we
174 used a cosine spatial growth stretch distribution and examined how buckling was affected
175 when system stiffness ($\hat{k}$) was varied between 0.5 and 1.5. We found that for identical
176 distributions of growth, rod buckling varies locally as a function of stiffness (Fig. 2F),
177 suggesting that small changes at the cellular level could alter shape locally.
178
179 Taken together, our results indicate that growth and mechanical traits are sufficient to
180 describe the differences in meristem shape between WT and *clv* SAM. Furthermore, local
181 variations of these two parameters could suffice to lead to the local curvature defects
182 observed in *clv* meristems.
183
184 **Loss of *CLV* activity is associated with a reduction in epidermal cell stiffness**
185 Our models predicted that buckling in *clv* mutants is, at least in part, dependent on stiffness
186 changes in the SAM. We had previously shown that *CLV3*-expressing stem cells are stiffer
187 than PZ cells (Milani et al., 2014). However, because *WUS* expression in the underlying OC
188 is thought to be largely responsible for stem cell identity, and because *WUS* expression
189 expands throughout the L2 of *clv* mutants, it was unclear if cellular stiffness patterns could
190 indeed be altered in the mutant. To test this, we measured rigidity in epidermal cells in WT

191 and *clv3* SAM using an atomic force microscope (AFM), following the approaches that we
192 developed for WT shoot apices (Milani et al., 2014; Beauzamy et al., 2015). We scanned
193 regions of either 169 μm^2 pixels or 2750 μm^2 using a spherical tip with a radius of 400 nm
194 mounted on a cantilever with a nominal force constant of 42 $N.m^{-1}$. At each point, we applied
195 a force of 1 μN, corresponding to an indentation depth of 100-150 nm, as previously
196 published (Milani et al., 2014). The resulting force-displacement curves were used to
197 calculate the apparent Young's modulus at each point. These values were then corrected in
198 order to remove artefacts caused by local slope, particularly in *clv* mutant SAM (Fig. 3A-D).
199 We found that cells in WT SAM displayed an apparent Young's modulus of 12.16 $\pm$ 1.17
200 MPa (mean $\pm$ s. d.). On the other hand, *clv3-2* mutant SAM have an average apparent
201 Young's modulus of 9.63 $\pm$ 0.74 MPa, indicating that these cells are significantly softer than
202 the WT (Fig. 3E, Fig. S4). Similarly, compared to WT Col-0 plants, *clv1-8* meristems also
203 display significantly lower apparent Young's moduli (Col-0: 10.58 $\pm$ 0.38 MPa, *clv1-8*: 8.94
204 $\pm$ 0.45 MPa) (Fig. 3E, Fig. S4, Table S1). These results are consistent with those from our
205 analytical models, which suggest that reduced tissular stiffnesses can result in buckling,
206 hence in surface curvature defects.
207
208 **Functional domain separation is absent in *clv* SAM**
209 We reasoned that the local heterogeneities in growth and/or stiffness, as predicted by our
210 models, might be caused by variations in local genetic identity in cells of *clv* shoot apices.
211 While no previous studies have suggested that this is the case, neither did those studies
212 specifically examine *clv* meristems for such differences. To determine whether such
213 variations do indeed exist, we started by retesting the expression patterns of CZ and OC
214 markers using mRNA *in situ* hybridisation assays in WT and *clv3* mutant SAM. To examine
215 CZ identity, we tested several genes that had been identified as enriched in *CLV3*-
216 expressing cells (Yadav et al., 2009). We settled on the *APUM10* gene that encodes a
217 protein of the Puf family, whose conserved Pumillio homology domain regulates mRNA
218 stability and translation in eukaryotic cells, via its sequence-specific RNA binding (Tam et
219 al., 2010; Abbasi et al., 2011; Qiu et al., 2019). The precise function of APUM10 is unknown.
220 We used *WUS* to examine OC identity (Laux et al., 1996; Mayer et al., 1998).
221
222 *APUM10* is expressed in an approximately 8-cell domain at the centre of the SAM (Fig. 4A),
223 and *WUS* is expressed in an underlying group of cells (Fig. 4C). As expected in *clv3-2*
224 mutant SAM, we detect both *APUM10* and *WUS* in a broad domain occupying almost the
225 entire meristem, with *APUM10* expressed principally in the L2 layer (Fig. 4B, B'), while *WUS*

226 is expressed in deeper layers (Fig. 4D, D'). However, both genes are expressed in a
227 discontinuous manner, with patches of cells throughout the SAM not displaying any
228 detectable expression (Fig. 4B, D). A close inspection of similar work published by other
229 groups shows that such a patchy expression was visible, but had gone unnoticed (Brand et
230 al., 2000; Schuster et al., 2014).
231
232 It was unclear to us why some patches of cells in a *clv3* mutant might not express stem cell
233 or OC identity. We reasoned that such cells might instead express PZ markers. To test this,
234 we localised mRNA for the *MP* gene, which is expressed mainly in the PZ in the WT (Hardtke
235 and Berleth, 1998; Zhao et al., 2010) (Fig. 4E). In enlarged *clv3-2* SAM, the PZ is thought
236 to be restricted to areas adjacent to the flowers, well below the top of the SAM. However our
237 data reveal that in *clv* mutants, *MP* expression is also very broad, similar to the expression
238 patterns of the CZ and OC markers (Fig. 4F, F'). Strikingly, we also noted that patches of
239 cells are devoid of *MP* expression (Fig. 4F'). Taken together, our results suggest that
240 identities of the three key SAM zones are present in overlapping groups of cells in *clv3-2*
241 SAM. Furthermore, they are expressed discontinuously in the sub-epidermal cell layer,
242 which gives an impression of an overall patchiness. In short, the expression patterns of
243 *APUM10*, *MP*, and *WUS* are overlapping and do not set clear boundaries between functional
244 domains of the *clv3-2* SAM. They are rather patchy and spanning all over the enlarged SAM.
245
246 Because our results seemingly contradicted the prevailing view of *clv3* SAM being
247 composed entirely of stem cells (Brand et al., 2002; Busch et al., 2010; Dao et al., 2022;
248 Kwon et al., 2005; Lenhard and Laux, 2003; Ma et al., 2019; Müller et al., 2006; Nimchuk et
249 al., 2011; Whitewoods et al., 2018; Wu et al., 2005), we thought it possible that normal
250 domain organisation might exist at a more local level. In order to more closely investigate
251 the relative positioning of *APUM10*, *MP*, and *WUS* expression domains in *clv3* SAM, we
252 performed pairwise *in situ* hybridisations using alternating serial sections, with one probe
253 used on even-numbered sections, and the other on odd-numbered sections. Our results
254 indicate that in the WT, *APUM10* and *WUS* expression domains do not appear to overlap,
255 because *APUM10* is detected in the outer cell layers of the CZ whereas *WUS* is expressed
256 in deeper cells (Fig. 4G, G'). However in the *clv3-2* mutant, the expression domains largely
257 overlap across the entire SAM (Fig. 4H-I', Fig. S5), with a few zones where *APUM10* is
258 expressed and *WUS* is not (Fig. 4H', I'). Similarly, in the WT, *APUM10* and *MP* are
259 expressed in the mutually exclusive CZ and PZ domains, respectively (Fig. 4J, J'), whereas
260 in the *clv3-2* mutant, they are frequently observed together in cells of the SAM. However,

261 we sometimes detected patches of cells displaying only *MP* expression, as well as patches
262 of cells devoid of any signal of these genes (Fig. 4K-L', Fig. S6). Together, these results
263 show that *clv3* SAM comprise a heterogeneous group of cells with mixed genetic identities,
264 rather than a homogeneous population of stem cells resembling the cells located above the
265 WT OC. Furthermore, we observed similar expression patterns in SAM from other alleles of
266 *clv1* and *clv3* (Fig. S7), suggesting that chimeric cell identities are a general feature of
267 fasciated *clv* meristems.
268
269 **Exogenous auxin elicits a strong response throughout the *clv3* meristem**

270 Given that cells in fasciated *clv3* SAM show traits not usually associated with stem cells,
271 such as chimeric cell identities, and reduced stiffness, we wondered if they are also
272 functionally different from stem cells. We wished to use auxin response as a functional test
273 in *clv* mutants for the following reasons. First, it has long been thought that a key aspect of
274 organogenesis at the shoot apex is the presence of a CZ that is insensitive to auxin signalling
275 (de Reuille et al., 2006; Douady and Couder, 1996; Galvan-Ampudia et al., 2020; Vernoux
276 et al., 2011). Thus auxin insensitivity could conceivably be used as a readout for cell identity
277 in the SAM. Secondly, anecdotal evidence indicates that unlike WT plants, *clv3* mutants
278 grown in the presence of the auxin transport inhibitor N-1-naphthylphthalamic acid, never
279 show escapers that form lateral organs (O. Hamant and T. Vernoux, personal
280 communication), suggesting an interaction between the CLV and auxin pathways. Lastly,
281 recent work has shown that MP regulates the polar subcellular localisation of the PIN1 auxin
282 efflux transporter, which promotes auxin accumulation and drives organogenesis (Bhatia et
283 al., 2016). Since *MP* is misregulated in *clv* mutants, it is possible that auxin fluxes are
284 perturbed and that organogenesis is affected.
285
286 In order to directly test how *clv3* shoot apices respond to auxin, we treated WT and *clv3-2*
287 SAM with exogenous auxin for 5 hours as described (Galvan-Ampudia et al., 2020), and
288 observed the expression of the *pDR5rev::GFPer* auxin signalling reporter approximately 7
289 and 25 hours after the start of treatment. In WT samples prior to treatment, *DR5* expression
290 is visible in the L1 of the SAM, but not in the CZ (Fig. 5A, D). 7 h after the end of auxin
291 treatment, WT SAM display moderate GFP expression in large portions of the PZ and in
292 internal layers, with no expression observed in the CZ (Fig. 5B, E). At 25 h, we observed
293 high levels of GFP throughout the PZ and in internal layers, and almost none in the CZ (Fig.
294 5C, F). Similar results are observed in floral meristems, with high expression in the PZ and
295 in internal layers, and none in the CZ (Fig. 5B-C, E-F). In untreated *clv3-2* samples, *DR5*

296 expression was different from the WT, in that we detected no GFP in the bulk of the enlarged
297 SAM, with the exception of a few L1 cells (Fig. 5G, J, M, P). After treatment with auxin, *clv3*
298 mutants responded in one of two ways. In the first group (n = 4 out of 6) *DR5* expression in
299 the SAM was increased in the inner layers, but not in the L1 at 6 h (Fig. 5H, K), and this
300 trend was further enhanced at 25 h (Fig. 5I-L). In the second group (n = 2 out of 6), we
301 observed a mild increase in *DR5* expression in the SAM at 6 h (Fig. 5N, Q), whereas at 25
302 h, high GFP expression was detected throughout the SAM (Fig. 5O, R). In *clv3* flowers prior
303 to treatment, small patches of *DR5* expression were observed, whereas after treatment, high
304 levels of expression were detected throughout all floral meristems, with no evident zone of
305 exclusion representing a putative CZ, as in the WT (Fig. 5M-O). Taken together, these
306 results show that cells in *clv* mutant SAM are capable of responding to auxin signalling, an
307 output more associated with WT PZ, rather than CZ, cells. These data also indicate that
308 auxin distribution and/or the capacity for proper auxin signalling are disrupted in fasciated
309 *clv* SAM.
310
311
312 **Discussion**
313 The loss of *CLV* activity in *Arabidopsis* shoot apical stem cells leads to the development of
314 fasciated meristems, a phenotype broadly interpreted as being caused by a massive
315 increase in stem cell numbers. Direct experimental evidence for this, as far as we can
316 ascertain, comes from a *CLV3* transcriptional reporter (Brand et al., 2002; Reddy and
317 Meyerowitz, 2005) that is expressed throughout the enlarged meristem of *clv3* mutants.
318 However, given that WUS is broadly expressed throughout the L2 of *clv* mutants, that it is
319 sufficient to activate *CLV3* expression (Schoof et al., 2000), and that it does so by directly
320 binding the *CLV3* promoter (Yadav et al., 2011), it is unsurprising that a *CLV3* transcriptional
321 reporter would be broadly expressed in *clv* meristems. Thus the *CLV3* reporter is not an
322 appropriate marker to study cell identity in *clv* mutants.
323
324 An alternate way of deciphering regional identities in *clv* mutants is by characterising cellular
325 properties. One study suggested that *clv* L1 cells are slightly smaller than the WT, while L2
326 cells are slightly larger (Laufs et al., 1998), while another hinted that *clv* L1 cells are likely
327 larger than the WT (Schoof et al., 2000). However, that analysis was based on inter-nuclear
328 distances and only provided a rough estimate of cell size. In this manuscript, we use more
329 recently-developed approaches (Fernandez et al., 2010; Barbier de Reuille et al., 2015; Kiss
330 et al., 2017) to quantify cell volumes, areas and surface curvatures. Our findings show that

the size of subepidermal cells in *clv* mutant SAM are much larger than in the WT, and resemble certain WT L3 cells, such as those in the potential OC (Fernandez et al., 2010). Curiously, this observation is reminiscent of previous findings that floral meristems lack one of the two layers of the tunica with respect to the SAM (Popham, 1951). The effect of this volume change in L2 cells on meristem structure is difficult to estimate. One possibility is that the abrupt change in cell size generates a higher frequency of cell boundary overlaps between the L1 and L2, which in turn could create a more fragile structure, akin to building a wall with smaller cells in one layer and much larger bricks in the next. The tissue buckling we observe could be located around such regions.

Over the past 15 years, several groups have generated reaction-diffusion or other biochemical computational models to study how a stable CLV-WUS feedback pattern is maintained in the SAM (Jönsson et al., 2005; Jönsson et al., 2006; Fujita et al., 2011; Chickarmane et al., 2012; Gruel et al., 2016; Klawe et al., 2020; Plong et al., 2021; Battogtokh and Tyson, 2022). However, because these studies were mostly carried out in the absence of cell division rules, they have not needed to address the mechanical constraints created by growth. Similarly, models of phyllotaxis at the shoot apex have also mostly favoured addressing how purely biochemical events underlie the distinct auxin accumulation patterns that lead to organogenesis (Reinhardt et al., 2000; Vernoux et al., 2000; Heisler et al., 2005; Galvan-Ampudia et al., 2020). Our analytical model, on the other hand, attempts to explain morphology through a mechanical framework. The model shows that differences in mechanical properties, alone or in combination with differences in growth rates, can explain tissue buckling. Furthermore, local mechanical or growth heterogeneities are sufficient to describe the buckling phenotypes of *clv* SAM.

Certain *clv* alleles do not display the line fasciation exhibited by alleles used in this study, but instead exhibit point fasciation, a milder phenotype where the SAM is a broader and taller dome with respect to the wild type (Clark et al., 1993; Laufs et al., 1998; Schoof et al., 2000). Our modelling analyses indicate that when growth is only slightly increased, the resulting phenotype is one of tissue bulging without significant buckling (Fig. 2A curve for γ^* = 8.99). In this manner, a weaker *clv* allele, or indeed a single mutant as compared to a multiple knock-out (Dao et al., 2022), might impose a lower increase in cellular growth rate that, when combined with sufficient residual stiffness, could temper the phenotype by preventing massive overproliferation, thus leading to a less dramatic fasciation than the stronger alleles examined in this study.

One specificity in our models is that we do not directly address absolute cell stiffness in the different layers, but rather utilise a ratio of stiffness between the inner and outer layers to examine system behaviour. Because it is currently challenging to ascertain cell stiffness in inner layers, we cannot directly confront our model. However, stiffness can be measured with some accuracy in the outer layer. Because the literature suggests that all L1 cells in *clv* SAM have stem cell identity, and because *CLV3*-expressing cells are stiffer than PZ cells, we had predicted that L1 cells in the enlarged *clv* SAM would display higher stiffness compared to WT cells. However, our measurements showed that *clv* L1 cells are consistently less stiff than the WT. Our results thus indicate that cells in *clv* SAM are qualitatively different to those found in the CZ or PZ of wild-type SAM.

A recent study has revealed a link between the number of neighbours for any given cell (neighbour number) and cell size, and how they influence tissue patterning (Long et al., 2020), showing that turgor pressure is anticorrelated to cell size and neighbour number, and that pressure correlates with growth. Thus smaller cells tend to have fewer neighbours, and display lower pressure and higher growth. Therefore the larger cells of the L2 layer of *clv* mutants might be less stiff than the L1, which is itself less stiff than the CZ or PZ of the WT. This is consistent with the predictions from our analytical models, which suggest that buckling occurs when the inner layers are less stiff than the L1 (Cao and Hutchinson, 2012; Cerda and Mahadevan, 2003). An experimental validation of this would require the use of techniques to measure stiffness or pressure in internal layers.

Several articles have revealed that tissue-level shape robustness emerges from cell growth and size variability averaged through space and time (Hervieux et al., 2016; Hong et al., 2016; Kamimoto et al., 2016; Tsugawa et al., 2017; Long et al., 2020). The local mechanical and growth heterogeneities predicted by our models are likely to be principally caused by perturbed genetic patterns in *clv* mutants. Our results show that unlike in WT SAM, which display a clear separation of functional domains and associated gene expression patterns, cells in *clv* SAM bear identities that are chimeric and variable. Cells in *clv* SAM display various abnormal combinations of CZ, OC and PZ identity, with each of them expressed non-uniformly within the meristem. This patchiness is visible in certain mRNA *in situ* localisation data on *clv* SAM in the literature (Brand et al., 2000; Schoof et al., 2000; Reddy and Meyerowitz, 2005; Schlegel et al., 2021), but has not been accorded much importance.

400 It is unclear precisely how such a mixed pattern arises and what the exact consequences
401 might be.
402
403 We propose that cell function is differentially regulated in cells with differing chimeric
404 identities, leading to varying growth or mechanical properties, which in turn alter
405 morphogenesis at the tissue level. Our data suggest that the bulk of the cells in *clv* SAM are
406 in fact capable of responding to exogenous auxin treatment, which resembles the behaviour
407 of PZ, rather than CZ, cells. However, these chimeric *clv* cells clearly do not undergo
408 differentiation. Because the tight regulation of auxin accumulation in space and time is
409 crucial for proper organogenesis (Reinhardt et al., 2000; Vernoux et al., 2000; Heisler et al.,
410 2005; Galvan-Ampudia et al., 2020), one possibility is that auxin regulation is also perturbed
411 in *clv* SAM. It may be that the abnormal shape of the mutant SAM does not allow proper
412 auxin accumulation patterns to be generated. Alternatively, CLV signalling could regulate
413 auxin activity more directly, such as in the moss (Nemec-Venza et al., 2022). A detailed
414 analysis of auxin fluxes and auxin signalling, particularly during vegetative growth in *clv*
415 mutants, will be essential for a full understanding of the role of auxin in fasciation.
416
417 Taken together, our data strongly suggest that cells in fasciated *clv* meristems do not fit the
418 current definition of true stem cells. Alternatively, it is possible that cellular identities in
419 mutants with perturbed stem cell regulation are fluid. It could also be that such fluid or
420 chimeric identities also exist in the wild type, for instance at CZ-PZ or PZ-flower boundaries.
421 It is possible that our current definition of stem cells is too restrictive, and needs to be
422 expanded to include not only genetic, but also mechanical and functional parameters. Better
423 reporters for diverse cellular properties, as well as a detailed real-time analysis, will be
424 necessary to resolve how such chimeric identities arise and what their effects are on plant
425 architecture.
426
427 **Materials and methods**
428 *Plant material and culture conditions*
429 The following plant lines were used in this study: L*er* and Col-0 as wild types, *clv3-2* (Clark
430 et al., 1995), *clv3-7* (Fletcher et al., 1999), *clv1-8* (Medford et al., 1992), *pCLV3::GFPer*
431 (Reddy and Meyerowitz, 2005), *pDR5rev::GFPer* (Friml et al., 2003), *pDR5::3xVENUS-N7*
432 (Vernoux et al., 2011), and *pUBQ10::LTI6b-TdTomato* (Shapiro et al., 2015).
433

434 Seeds were sown on soil, and placed in short-day conditions (8 hrs light, 20°C, 50-60%
435 humidity and 16 hrs dark, 16°C, 50-60% humidity) for ten days. Seedlings were then
436 transplanted into individual pots and placed back into the short-day conditions growth
437 chamber. One month after transplantation, plants were transferred from short-day to long-
438 day conditions (16 hrs light period, 20°C, 60% humidity and 8 hrs dark period, 19°C, 60%
439 humidity) until flowering. The light sources were LED fixtures (Valoya, C75, spectrum NS12),
440 with an intensity of 150 $\mu mol.m^{-2}.s^{-1}$.
441
442 *RNA in situ hybridisations*
443 RNA *in situ* hybridisations on sections were performed according to published protocols
444 (Long et al., 1996). Dissected meristems were fixed in FAA (formaldehyde 3.7% [v/v],
445 ethanol 50% [v/v], acetic acid 5% [v/v], H_2O to final volume), washed, dehydrated and
446 embedded in paraplast. Embedded samples were cut (10 µm-thick) and attached to pre-
447 coated glass slides (Superfrost Plus Gold, Fisher Scientific). Antisense probes were made
448 from PCR products using cDNA from inflorescences as a template, except for *CLV3*, which
449 was amplified using genomic DNA. Those PCR products were transcribed into RNA and
450 then labelled using digoxigenin (DIG)-UTP. All probes were filtered on columns (CHROMA
451 SPIN-30 columns, Clontech) to remove remaining nucleotides. Immunodetection was
452 performed using an anti-DIG antibody coupled to alkaline phosphatase (Anti-Digoxygenin-
453 AP, Fab fragments), whose activity was detected by the chromogenic method using
454 NBT/BCIP (Roche). Sections were finally washed with water and observed under a Zeiss
455 Imager M2 microscope equipped with an AxioCam Mrc camera, and 10 X or 20 X objectives
456 in DIC (differential interference contrast) mode.
457
458 *Plant dissection and preparation for confocal microscopy*
459 SAM were grown on soil and dissected soon after bolting. An approximately 1 cm region at
460 the apex of the stem was placed in apex culture medium (ACM: ½ MS medium, 1% [w/v]
461 sucrose, pH adjusted to 5.8 with 1M KOH, 0.8% [w/v] agarose, supplemented with 1X
462 vitamins (1000X stock: 5 g myo-inositol, 0.05 g nicotinic acid, 640.05 g pyridoxine
463 hydrochloride (B6), 0.5 g thiamine hydrochloride (B1), 0.1 g glycine, H_2O to 50 mL, filter
464 before aliquoting) and cytokinins (BAP; 125-175 nM final)), and flower buds were removed
465 until the shoot meristem was sufficiently exposed for proper imaging. Dissected samples
466 were placed in a growth cabinet under long-day conditions until confocal observation.
467

468 *Confocal imaging*

469 Imaging was carried out on a Leica TCS SP8 (DM6000 CS) upright confocal laser scanning
470 microscope, equipped with a 25x water dipping lens (Leica HC FLUOTAR L 25x/0.95 W
471 VISIR) and a Leica HyD hybrid detector. FM4-64 (ThermoFisher Scientific, T13320) was
472 used to mark the plasma membrane as previously described (Fernandez et al., 2010). It was
473 excited with a 488 nm laser diode and detected at 600-640 nm. GFP was excited at 488 nm
474 and detected at 500-520 nm. VENUS was excited at 514 nm and detected at 520-535 nm.
475 tdTomato was excited at either 514 or 552 nm and detected at 560-600 nm.
476

477 *Image analysis*

478 Confocal images were analysed with Fiji (Schindelin et al., 2012). Fiji was used to generate
479 2D projections from 3D confocal stacks (3D viewer plugin) and to generate orthogonal slices.
480

481 3D reconstructions of confocal stacks were generated using the MARS pipeline (Fernandez
482 et al., 2010). Shoot meristems were imaged from three or four different angles by means of
483 a custom-made device to tilt and/or rotate the sample by 15-20 degrees between
484 acquisitions. These images were then fused using MARS and the external contours of the
485 sample were detected using the Level Set Method (Kiss et al., 2017). This contour, along
486 with the 3D reconstructed sample to generate cell-segmented images in 3D using a
487 watershed segmentation algorithm. Cells were then extracted from the segmented image
488 for the L1 and L2 tissue layers and the volume of each cell was calculated.
489

490 *Cell area measurements*

491 Cell areas were extracted by analysing individual image stacks, focussing on the region of
492 the tissue orthogonal to the axis of the image. We determined the midline of the small group
493 of cells within each layer near the centre of the image. These individual slices were then
494 segmented and cell areas determined using MorphoGraphX (Barbier de Reuille et al., 2015;
495 Kiss et al., 2017). We finally used R to plot the data and run statistical tests.
496

497 *Computation of SAM curvature*

498 Tissue surface curvature measurements were made using MorphoGraphX (MGX) (Barbier
499 de Reuille et al., 2015; Kiss et al., 2017). The LSM contour for each 3D MARS-reconstructed
500 sample (see above) was used to first generate a mesh and the Gaussian curvature was
501 calculated for a 10-pixel radius for each pixel in the image.

502

503 *Statistical analysis*

504 Plots and statistical analyses were done in the R environment (Posit team, 2023). Welch's
505 t-tests were used to compare the mean of two independent groups: cell areas and cell
506 volumes in different cell layers, and the apparent Young's modulus in WT and mutant SAM.
507 When we use boxplots, the boxes extend from the first to the third quartile and the whiskers
508 from 10% to 90% of the values, the solid black line represents the median of the distribution.
509 Throughout the manuscript, average values are means $\pm$ s.d.

510

511 *Hormone treatments*

512 Auxin treatments were performed by immersing dissected SAM into 1mM Indole-3-acetic
513 acid (IAA) solution (Sigma, 0.2 M IAA stock, extemporaneously diluted 1:200 in H_2O). For
514 consistency, the treatment was started prior to 7.30 A.M. and lasted for five hours as
515 described (Galvan-Ampudia et al., 2020). The IAA solution was changed midway. Samples
516 were then imaged by confocal microscopy five, 12 and 30 hours post-treatment to follow
517 DR5 reporter expression dynamics.

518

519 *Analytical models*

520 See supplementary methods.

521

522 *Atomic force microscopy (AFM) and data analysis*

523 The day before the experiment, SAM were dissected to remove all flower buds older than
524 stage 3 that hindered access to the meristem. The samples were placed into 50 mm plastic
525 Petri dishes filled with ACM, and grown overnight in a growth cabinet with long-day
526 conditions. SAM were stained with FM4-64 and imaged with a Leica TCS SP8 (DM600 CS)
527 upright confocal laser scanning microscope to collect cell contours.

528

529 AFM experiments were performed on a stand-alone JPK Nanowizard III microscope
530 equipped with a CellHesion module and a 100 µm-range Z piezo driven by a JPK
531 Nanowizard software 6.0. The acquisitions were done in Quantitative Imaging mode (QI).
532 The experiments were performed in distilled water at room temperature. We used a silica
533 spherical tip (Special Development SD-sphere-NCH, Nanosensors) mounted on a silicon
534 cantilever with a nominal force constant of 42 $N.m^{-1}$, and a radius of 400 nm. Scan size was
535 generally within 45 and 60 µm (even if in one case we went up to 80 µm, but smaller scans
536 are faster and prevent growth to impact the imaging) with pixel size of approximately 500

537 nm (e.g. 96 x 96 pixels for 45 µm scan size). The applied force trigger was 1 µN, a force
538 corresponding to 100-150 nm indentation, in order to indent the cell wall only (Milani et al.,
539 2011; Tvergaard and Needleman, 2018). The ramp size was 2 µm, approach speed was 10
540 $\mu m.s^{-1}$ and retraction speed 100 $\mu m.s^{-1}$.
541 Cantilever calibration was performed following the standard thermal noise method. We
542 measured the deflection sensitivity by doing a linear fit of the contact part of a force curve
543 acquired on sapphire in phosphate-buffered saline (PBS). Then, we determined the spring
544 constant by acquiring the thermal noise spectrum of the cantilever and fitting the first normal
545 mode peak using a single harmonic oscillator model. The same tip was used for several
546 experiments in different days as long as possible. In order to reduce the offsets in force that
547 can be introduced by each new calibration, especially by the measurements of the deflection
548 sensitivity, we followed the SNAP protocol (Schillers et al., 2017).
549
550 Data analysis was done using JPK Data Processing software 6.0. Force vs height curves
551 were first flattened by removing the result of a linear fit done over a portion of the baseline,
552 in order to set this part to 0 force. A first estimation of the point of contact (POC), was
553 obtained considering the first point crossing the 0 of forces, starting from the end of the
554 approach curve (i.e. trigger force position). The force vs. tip-sample distance was then
555 obtained calculating a new axis of distances as Height [m] – tip deflection Δz [m]. Young's
556 modulus was obtained by fitting the entire force vs tip-sample distance curves (note that we
557 used approach curves) with a Hertz model (referred to as Paraboloid in JPK Data
558 Processing). For our analysis, we used a tip radius R of 400 nm and a Poisson's ratio v of
559 0.5 (as it is conventionally set for biological material in the literature (Kulkarni et al., 2018)),
560 where the Young's modulus, the POC and an offset in force were kept as free parameters
561 of the fit. A preliminary filtering step was performed to exclude data points associated with
562 α, the angle between the normal to the surface and the z direction, superior or equal to 55°.
563 This threshold was set based on the distribution of angles in all samples. In addition, a non
564 systematic second filtering step was applied on samples containing artefacts on their
565 surface, such as dust particles. The threshold criteria aims at removing data that are not well
566 processed by the Hertz model. Thus, the data with the 10% highest residuals root mean
567 square values were excluded.
568
569 Finally, we removed or reduced the effect of the local slope in our calculations by adapting
570 a formula from the literature (Routier-Kierzkowska et al., 2012), thus leading to the following
571 corrected apparent Young's modulus equation:

$$E_n = E_z(1 + p^2)^{\frac{5}{4}}, (1).$$

With E_n the corrected apparent Young's modulus in the direction normal to the surface, E_z the Young's modulus in the z direction, and $p = tan(\alpha)$, with α being the angle between the normal to the surface and the z direction.

Acknowledgements

We thank V. Mirabet and N. Dubrulle for help with preliminary AFM measurements, A. Kiss for help with 3D segmentations and surface curvature detection, and G. Gilbert for help with *in situ* hybridisations. We thank the PLATIM/LyMIC imaging facility of the SFR Biosciences (UMS3444/CNRS, US8/Inserm, ENS de Lyon, UCBL1). We thank A. Lacroix, J. Berger, P. Bolland, H. Leyral, and I. Desbouchages for assistance with plant growth and logistics. This article is based on LRL's PhD thesis: Rambaud-Lavigne, L. E. S. (2018), The genetics and mechanics of stem cells at the Arabidopsis shoot apex. *PhD thesis*, University of Lyon, Lyon, France, downloadable at: theses.hal.science/tel-02366972.

Author contributions

Conceptualization: LRL, AB, PD; Methodology: AC, NG, SB, AB; Software & Modeling: AC, NG; Validation: LRL, VB, PD; Formal Analysis: QL, AC, LRL, PD; Investigation: LRL, SB, VB, PD; Data Curation: LRL, PD; Writing - Original Draft Preparation: LRL, AC, NG, PD; Writing - Review & Editing: LRL, AC, SB, NG, AB, PD; Visualisation: LRL, AC, QL, NG, PD; Supervision: NG, AB, PD; Funding Acquisition: LRL, NG, PD.

Competing interests

No competing interests declared.

Funding

This work was supported by a PhD fellowship from the Ecole Normale Supérieure de Lyon (ENSL) to LRL., and a Science Engineering Research Board grant (SERB-POWER) to NG.

Data availability

All datasets and scripts will be made available before publication.

References

Abbasi, N., Park, Y.-I. and Choi, S.-B. (2011). Pumilio Puf domain RNA-binding proteins in Arabidopsis. *Plant Signal. Behav.* **6**, 364–368.

Aggarwal, P., Yadav, R. K. and Reddy, G. V. (2010). Identification of novel markers for stem-cell niche of Arabidopsis shoot apex. *Gene Expr. Patterns* **10**, 259–264.

Barbier de Reuille, P., Routier-Kierzkowska, A.-L., Kierzkowski, D., Bassel, G. W., Schüpbach, T., Tauriello, G., Bajpai, N., Strauss, S., Weber, A., Kiss, A., et al. (2015). MorphoGraphX: A platform for quantifying morphogenesis in 4D. *eLife* **4**, 05864.

Battogtokh, D. and Tyson, J. J. (2022). Nucleation of stem cell domains in a bistable activator-inhibitor model of the shoot apical meristem. *Chaos Woodbury N* **32**, 093117.

Beauzamy, L., Louveaux, M., Hamant, O. and Boudaoud, A. (2015). Mechanically, the Shoot Apical Meristem of Arabidopsis Behaves like a Shell Inflated by a Pressure of About 1 MPa. *Front. Plant Sci.* **6**,.

Berleth, T. and Jürgens, G. (1993). The role of the monopteros gene in organising the basal body region of the Arabidopsis embryo. *Development* **118**, 575–587.

Bhatia, N., Bozorg, B., Larsson, A., Ohno, C., Jönsson, H. and Heisler, M. G. (2016). Auxin Acts through MONOPTEROS to Regulate Plant Cell Polarity and Pattern Phyllotaxis. *Curr. Biol.* **26**, 3202–3208.

Brand, U., Fletcher, J. C., Hobe, M., Meyerowitz, E. M. and Simon, R. (2000). Dependence of Stem Cell Fate in Arabidopsis on a Feedback Loop Regulated by CLV3 Activity. *Science* **289**, 617–619.

Brand, U., Grünewald, M., Hobe, M. and Simon, R. (2002). Regulation of CLV3 Expression by Two Homeobox Genes in Arabidopsis. *Plant Physiol.* **129**, 565–575.

Busch, W., Miotk, A., Ariel, F. D., Zhao, Z., Forner, J., Daum, G., Suzaki, T., Schuster, C., Schultheiss, S. J., Leibfried, A., et al. (2010). Transcriptional Control of a Plant Stem Cell Niche. *Dev. Cell* **18**, 841–853.

Cao, Y. and Hutchinson, J. W. (2012). Wrinkling Phenomena in Neo-Hookean Film/Substrate Bilayers. *J. Appl. Mech.* **79**,.

Cerda, E. and Mahadevan, L. (2003). Geometry and Physics of Wrinkling. *Phys. Rev. Lett.* **90**, 074302.

Chickarmane, V. S., Gordon, S. P., Tarr, P. T., Heisler, M. G. and Meyerowitz, E. M. (2012). Cytokinin signaling as a positional cue for patterning the apical–basal axis of the growing Arabidopsis shoot meristem. *Proc. Natl. Acad. Sci. U. S. A.* **109**, 4002–4007.

Clark, S. E., Running, M. P. and Meyerowitz, E. M. (1993). CLAVATA1, a regulator of meristem and flower development in Arabidopsis. *Development* **119**, 397–418.

Clark, S. E., Running, M. P. and Meyerowitz, E. M. (1995). CLAVATA3 is a specific regulator of shoot and floral meristem development affecting the same processes as CLAVATA1. *Development* **121**, 2057–2067.

Clark, S. E., Williams, R. W. and Meyerowitz, E. M. (1997). The CLAVATA1 gene encodes a putative receptor kinase that controls shoot and floral meristem size in Arabidopsis. *Cell* **89**, 575–585.

Dao, T. Q., Weksler, N., Liu, H. M.-H., Leiboff, S. and Fletcher, J. C. (2022). Interactive CLV3, CLE16 and CLE17 signaling mediates stem cell homeostasis in the Arabidopsis shoot apical meristem. *Development* **149**, dev200787.

Daum, G., Medzihradszky, A., Suzaki, T. and Lohmann, J. U. (2014). A mechanistic framework for noncell autonomous stem cell induction in Arabidopsis. *Proc. Natl. Acad. Sci.* **111**, 14619–14624.

de Reuille, P. B., Bohn-Courseau, I., Ljung, K., Morin, H., Carraro, N., Godin, C. and Traas, J. (2006). Computer simulations reveal properties of the cell-cell signaling network at the shoot apex in Arabidopsis. *Proc. Natl. Acad. Sci. U. S. A.* **103**, 1627–1632.

Douady, S. and Couder, Y. (1996). Phyllotaxis as a Dynamical Self Organizing Process Part II: The Spontaneous Formation of a Periodicity and the Coexistence of Spiral and Whorled Patterns. *J. Theor. Biol.* **178**, 275–294.

Fernandez, R., Das, P., Mirabet, V., Moscardi, E., Traas, J., Verdeil, J.-L., Malandain, G. and Godin, C. (2010). Imaging plant growth in 4D: robust tissue reconstruction and lineaging at cell resolution. *Nat. Methods* **7**, 547–553.

Fletcher, J. C., Brand, U., Running, M. P., Simon, R. and Meyerowitz, E. M. (1999). Signaling of Cell Fate Decisions by CLAVATA3 in Arabidopsis Shoot Meristems. *Science* **283**, 1911–1914.

Friml, J., Vieten, A., Sauer, M., Weijers, D., Schwarz, H., Hamann, T., Offringa, R. and Jürgens, G. (2003). Efflux-dependent auxin gradients establish the apical–basal axis of Arabidopsis. *Nature* **426**, 147–153.

Fujita, M., Himmelspach, R., Hocart, C. H., Williamson, R. E., Mansfield, S. D. and Wasteneys, G. O. (2011). Cortical microtubules optimize cell-wall crystallinity to drive unidirectional growth in Arabidopsis. *Plant J.* **66**, 915–928.

Galvan-Ampudia, C. S., Cerutti, G., Legrand, J., Brunoud, G., Martin-Arevalillo, R., Azais, R., Bayle, V., Moussu, S., Wenzl, C., Jaillais, Y., et al. (2020). Temporal integration of auxin information for the regulation of patterning. *eLife* **9**, e55832.

Gordon, S. P., Chickarmane, V. S., Ohno, C. and Meyerowitz, E. M. (2009). Multiple feedback loops through cytokinin signaling control stem cell number within the Arabidopsis shoot meristem. *Proc. Natl. Acad. Sci.* **106**, 16529–16534.

Goriely, A. (2017). *The Mathematics and Mechanics of Biological Growth*. New York, NY: Springer New York.

Gruel, J., Landrein, B., Tarr, P., Schuster, C., Refahi, Y., Sampathkumar, A., Hamant, O., Meyerowitz, E. M. and Jo nsson, H. (2016). An epidermis-driven mechanism positions and scales stem cell niches in plants. *Sci. Adv.* **2**, e1500989–e1500989.

Hardtke, C. S. and Berleth, T. (1998). The Arabidopsis gene MONOPTEROS encodes a transcription factor mediating embryo axis formation and vascular development. *EMBO J.* **17**, 1405–1411.

Heisler, M. G., Ohno, C., Das, P., Sieber, P., Reddy, G. V., Long, J. A. and Meyerowitz, E. M. (2005). Patterns of Auxin Transport and Gene Expression during Primordium Development Revealed by Live Imaging of the Arabidopsis Inflorescence Meristem. *Curr. Biol.* **15**, 1899–1911.

Hervieux, N., Dumond, M., Sapala, A., Routier-Kierzkowska, A.-L., Kierzkowski, D., Roeder, A. H. K., Smith, R. S., Boudaoud, A. and Hamant, O. (2016). A Mechanical Feedback Restricts Sepal Growth and Shape in Arabidopsis. *Curr. Biol.*

Hong, L., Dumond, M., Tsugawa, S., Sapala, A., Routier-Kierzkowska, A.-L., Zhou, Y., Chen, C., Kiss, A., Zhu, M., Hamant, O., et al. (2016). Variable Cell Growth Yields Reproducible Organ Development through Spatiotemporal Averaging. *Dev. Cell* **38**, 15–32.

Jeong, S., Trotochaud, A. E. and Clark, S. E. (1999). The Arabidopsis CLAVATA2 Gene Encodes a Receptor-like Protein Required for the Stability of the CLAVATA1 Receptor-like Kinase. *Plant Cell* **11**, 1925–1933.

Jönsson, H., Heisler, M., Reddy, G. V., Agrawal, V., Gor, V., Shapiro, B. E., Mjolsness, E. and Meyerowitz, E. M. (2005). Modeling the organization of the WUSCHEL expression domain in the shoot apical meristem. *Bioinforma. Oxf. Engl.* **21 Suppl 1**, i232-240.

Jönsson, H., Heisler, M. G., Shapiro, B. E., Meyerowitz, E. M. and Mjolsness, E. (2006). An auxin-driven polarized transport model for phyllotaxis. *Proc. Natl. Acad. Sci. U. S. A.* **103**, 1633–1638.

Kamimoto, K., Kaneko, K., Kok, C. Y.-Y., Okada, H., Miyajima, A. and Itoh, T. (2016). Heterogeneity and stochastic growth regulation of biliary epithelial cells dictate dynamic epithelial tissue remodeling. *eLife* **5**, e15034.

Kayes, J. M. and Clark, S. E. (1998). CLAVATA2, a regulator of meristem and organ development in Arabidopsis. *Development* **125**, 3843–3851.

Kiss, A., Moreau, T., Mirabet, V., Calugaru, C. I., Boudaoud, A. and Das, P. (2017). Segmentation of 3D images of plant tissues at multiple scales using the level set method. *Plant Methods* **13**,.

Klawe, F. Z., Stiehl, T., Bastian, P., Gaillochet, C., Lohmann, J. U. and Marciniak-Czochra, A. (2020). Mathematical modeling of plant cell fate transitions controlled by hormonal signals. *PLoS Comput. Biol.* **16**, e1007523.

Kulkarni, A. H., Chatterjee, A., Kondaiah, P. and Gundiah, N. (2018). TGF- *β* induces changes in breast cancer cell deformability. *Phys. Biol.* **15**, 065005.

Kwon, C. S., Chen, C. and Wagner, D. (2005). WUSCHEL is a primary target for transcriptional regulation by SPLAYED in dynamic control of stem cell fate in Arabidopsis. *Genes Dev.* **19**, 992–1003.

Laufs, P., Grandjean, O., Jonak, C., Kiêu, K. and Traas, J. (1998). Cellular parameters of the shoot apical meristem in Arabidopsis. *Plant Cell Online* **10**, 1375–1389.

Laux, T., Mayer, K. F., Berger, J. and Jurgens, G. (1996). The WUSCHEL gene is required for shoot and floral meristem integrity in Arabidopsis. *Development* **122**, 87–96.

Lenhard, M. and Laux, T. (2003). Stem cell homeostasis in the Arabidopsis shoot meristem is regulated by intercellular movement of CLAVATA3 and its sequestration by CLAVATA1. *Development* **130**, 3163–3173.

Lindsay, D. L., Sawhney, V. K. and Bonham-Smith, P. C. (2006). Cytokinin-induced changes in CLAVATA1 and WUSCHEL expression temporally coincide with altered floral development in Arabidopsis. *Plant Sci.* **170**, 1111–1117.

Long, J. A., Moan, E. I., Medford, J. I. and Barton, M. K. (1996). A member of the KNOTTED class of homeodomain proteins encoded by the STM gene of Arabidopsis. *Nature* **379**, 66–69.

Long, Y., Cheddadi, I., Mosca, G., Mirabet, V., Dumond, M., Kiss, A., Traas, J., Godin, C. and Boudaoud, A. (2020). Cellular Heterogeneity in Pressure and Growth Emerges from Tissue Topology and Geometry. *Curr. Biol.* **30**, 1504-1516.e8.

Luo, L., Zeng, J., Wu, H., Tian, Z. and Zhao, Z. (2018). A Molecular Framework for Auxin-Controlled Homeostasis of Shoot Stem Cells in Arabidopsis. *Mol. Plant* **11**, 899–913.

Ma, Y., Miotk, A., Šutiković, Z., Ermakova, O., Wenzl, C., Medzihradszky, A., Gaillochet, C., Forner, J., Utan, G., Brackmann, K., et al. (2019). WUSCHEL acts as an auxin response rheostat to maintain apical stem cells in Arabidopsis. *Nat. Commun.* **10**, 1–11.

Mayer, K. F., Schoof, H., Haecker, A., Lenhard, M., Jürgens, G. and Laux, T. (1998). Role of WUSCHEL in regulating stem cell fate in the Arabidopsis shoot meristem. *Cell* **95**, 805–815.

Medford, J. I., Behringer, F. J., Callos, J. D. and Feldmann, K. A. (1992). Normal and abnormal development in the Arabidopsis vegetative shoot apex. *Plant Cell* **4**, 631–643.

Milani, P., Gholamirad, M., Traas, J., Arnéodo, A., Boudaoud, A., Argoul, F. and Hamant, O. (2011). In vivo analysis of local wall stiffness at the shoot apical meristem in Arabidopsis using atomic force microscopy: Measuring wall stiffness in meristems with AFM. *Plant J.* **67**, 1116–1123.

Milani, P., Mirabet, V., Cellier, C., Rozier, F., Hamant, O., Das, P. and Boudaoud, A. (2014). Matching Patterns of Gene Expression to Mechanical Stiffness at Cell Resolution through Quantitative Tandem Epifluorescence and Nanoindentation. *PLANT Physiol.* **165**, 1399–1408.

Miwa, H., Betsuyaku, S., Iwamoto, K., Kinoshita, A., Fukuda, H. and Sawa, S. (2008). The Receptor-Like Kinase SOL2 Mediates CLE Signaling in Arabidopsis. *Plant Cell Physiol.* **49**, 1752–1757.

Müller, R., Borghi, L., Kwiatkowska, D., Laufs, P. and Simon, R. (2006). Dynamic and

Compensatory Responses of Arabidopsis Shoot and Floral Meristems to CLV3 Signaling. *Plant Cell* **18**, 1188–1198.

Müller, R., Bleckmann, A. and Simon, R. (2008). The Receptor Kinase CORYNE of *Arabidopsis* Transmits the Stem Cell–Limiting Signal CLAVATA3 Independently of CLAVATA1. *Plant Cell Online* **20**, 934–946.

Nemec-Venza, Z., Madden, C., Stewart, A., Liu, W., Novák, O., Pěnčík, A., Cuming, A. C., Kamisugi, Y. and Harrison, C. J. (2022). CLAVATA modulates auxin homeostasis and transport to regulate stem cell identity and plant shape in a moss. *New Phytol.* **234**, 149–163.

Nimchuk, Z. L., Tarr, P. T., Ohno, C., Qu, X. and Meyerowitz, E. M. (2011). Plant Stem Cell Signaling Involves Ligand-Dependent Trafficking of the CLAVATA1 Receptor Kinase. *Curr. Biol.* **21**, 345–352.

Plong, A., Rodriguez, K., Alber, M., Chen, W. and Reddy, G. V. (2021). CLAVATA3 mediated simultaneous control of transcriptional and post-translational processes provides robustness to the WUSCHEL gradient. *Nat. Commun.* **12**, 6361.

Popham, R. A. (1951). Principal Types of Vegetative Shoot Apex Organization in Vascular Plants. *Ohio J. Sci.* **51**, 249–269.

Posit team (2023). RStudio: Integrated Development Environment for R. Posit Software, PBC, Boston, MA. URL http://www.posit.co/.

Qiu, C., Dutcher, R. C., Porter, D. F., Arava, Y., Wickens, M. and Hall, T. M. T. (2019). Distinct RNA-binding modules in a single PUF protein cooperate to determine RNA specificity. *Nucleic Acids Res.* gkz583.

Reddy, G. V. and Meyerowitz, E. M. (2005). Stem-Cell Homeostasis and Growth Dynamics Can Be Uncoupled in the Arabidopsis Shoot Apex. *Science* **310**, 663–667.

Reinhardt, D., Mandel, T. and Kuhlemeier, C. (2000). Auxin Regulates the Initiation and Radial Position of Plant Lateral Organs. *Plant Cell* **12**, 507–518.

Routier-Kierzkowska, A.-L., Weber, A., Kochova, P., Felekis, D., Nelson, B. J., Kuhlemeier, C. and Smith, R. S. (2012). Cellular Force Microscopy for in Vivo Measurements of Plant Tissue Mechanics. *PLANT Physiol.* **158**, 1514–1522.

Schillers, H., Rianna, C., Schäpe, J., Luque, T., Doschke, H., Wälte, M., Uriarte, J. J., Campillo, N., Michanetzis, G. P. A., Bobrowska, J., et al. (2017). Standardized Nanomechanical Atomic Force Microscopy Procedure (SNAP) for Measuring Soft and Biological Samples. *Sci. Rep.* **7**,.

Schindelin, J., Arganda-Carreras, I., Frise, E., Kaynig, V., Longair, M., Pietzsch, T., Preibisch, S., Rueden, C., Saalfeld, S., Schmid, B., et al. (2012). Fiji: an open-source platform for biological-image analysis. *Nat. Methods* **9**, 676–682.

Schlegel, J., Denay, G., Wink, R. H., Pinto, K. G., Stahl, Y., Schmid, J., Blümke, P. and Simon, R. G. (2021). Control of Arabidopsis shoot stem cell homeostasis by two antagonistic CLE

peptide signalling pathways. *eLife* **10**, e70934.

Schoof, H., Lenhard, M., Haecker, A., Mayer, K. F. X., Jürgens, G. and Laux, T. (2000). The Stem Cell Population of Arabidopsis Shoot Meristems Is Maintained by a Regulatory Loop between the CLAVATA and WUSCHEL Genes. *Cell* **100**, 635–644.

Schuster, C., Gaillochet, C., Medzihradszky, A., Busch, W., Daum, G., Krebs, M., Kehle, A. and Lohmann, J. U. (2014). A Regulatory Framework for Shoot Stem Cell Control Integrating Metabolic, Transcriptional, and Phytohormone Signals. *Dev. Cell* **28**, 438–449.

Shapiro, B. E., Tobin, C., Mjolsness, E. and Meyerowitz, E. M. (2015). Analysis of cell division patterns in the *Arabidopsis* shoot apical meristem. *Proc. Natl. Acad. Sci.* **112**, 4815–4820.

Taguchi-Shiobara, F. (2001). The fasciated ear2 gene encodes a leucine-rich repeat receptor-like protein that regulates shoot meristem proliferation in maize. *Genes Dev.* **15**, 2755–2766.

Tam, P. P., Barrette-Ng, I. H., Simon, D. M., Tam, M. W., Ang, A. L. and Muench, D. G. (2010). The Puf family of RNA-binding proteins in plants: phylogeny, structural modeling, activity and subcellular localization. *BMC Plant Biol.* **10**, 44.

Tsugawa, S., Hervieux, N., Kierzkowski, D., Routier-Kierzkowska, A.-L., Sapala, A., Hamant, O., Smith, R. S., Roeder, A. H. K., Boudaoud, A. and Li, C.-B. (2017). Clones of cells switch from reduction to enhancement of size variability in Arabidopsis sepals. *Development* **144**, 4398–4405.

Tvergaard, V. and Needleman, A. (2018). Effect of Properties and Turgor Pressure on the Indentation Response of Plant Cells. *J. Appl. Mech.*

Vernoux, T., Kronenberger, J., Grandjean, O., Laufs, P. and Traas, J. (2000). PIN-FORMED 1 regulates cell fate at the periphery of the shoot apical meristem. *Development* **127**, 5157–5165.

Vernoux, T., Brunoud, G., Farcot, E., Morin, V., Van den Daele, H., Legrand, J., Oliva, M., Das, P., Larrieu, A., Wells, D., et al. (2011). The auxin signalling network translates dynamic input into robust patterning at the shoot apex. *Mol. Syst. Biol.* **7**, 508.

Whitewoods, C. D., Cammarata, J., Nemec Venza, Z., Sang, S., Crook, A. D., Aoyama, T., Wang, X. Y., Waller, M., Kamisugi, Y., Cuming, A. C., et al. (2018). CLAVATA Was a Genetic Novelty for the Morphological Innovation of 3D Growth in Land Plants. *Curr. Biol.*

Wu, X., Dabi, T. and Weigel, D. (2005). Requirement of Homeobox Gene STIMPY/WOX9 for Arabidopsis Meristem Growth and Maintenance. *Curr. Biol.* **15**, 436–440.

Yadav, R. K., Girke, T., Pasala, S., Xie, M. and Reddy, G. V. (2009). Gene expression map of the Arabidopsis shoot apical meristem stem cell niche. *Proc. Natl. Acad. Sci.* **106**, 4941–4946.

Yadav, R. K., Perales, M., Gruel, J., Girke, T., Jönsson, H. and Reddy, G. V. (2011). WUSCHEL protein movement mediates stem cell homeostasis in the Arabidopsis shoot apex. *Genes Dev.* **25**, 2025–2030.

Yamaguchi, N., Wu, M.-F., Winter, C. M., Berns, M. C., Nole-Wilson, S., Yamaguchi, A., Coupland, G., Krizek, B. A. and Wagner, D. (2013). A molecular framework for auxin-

mediated initiation of flower primordia. *Dev. Cell* **24**, 271–282.

Zhao, Z., Andersen, S. U., Ljung, K., Dolezal, K., Miotk, A., Schultheiss, S. J. and Lohmann, J. U. (2010). Hormonal control of the shoot stem-cell niche. *Nature* **465**, 1089–1092.

Figure 1

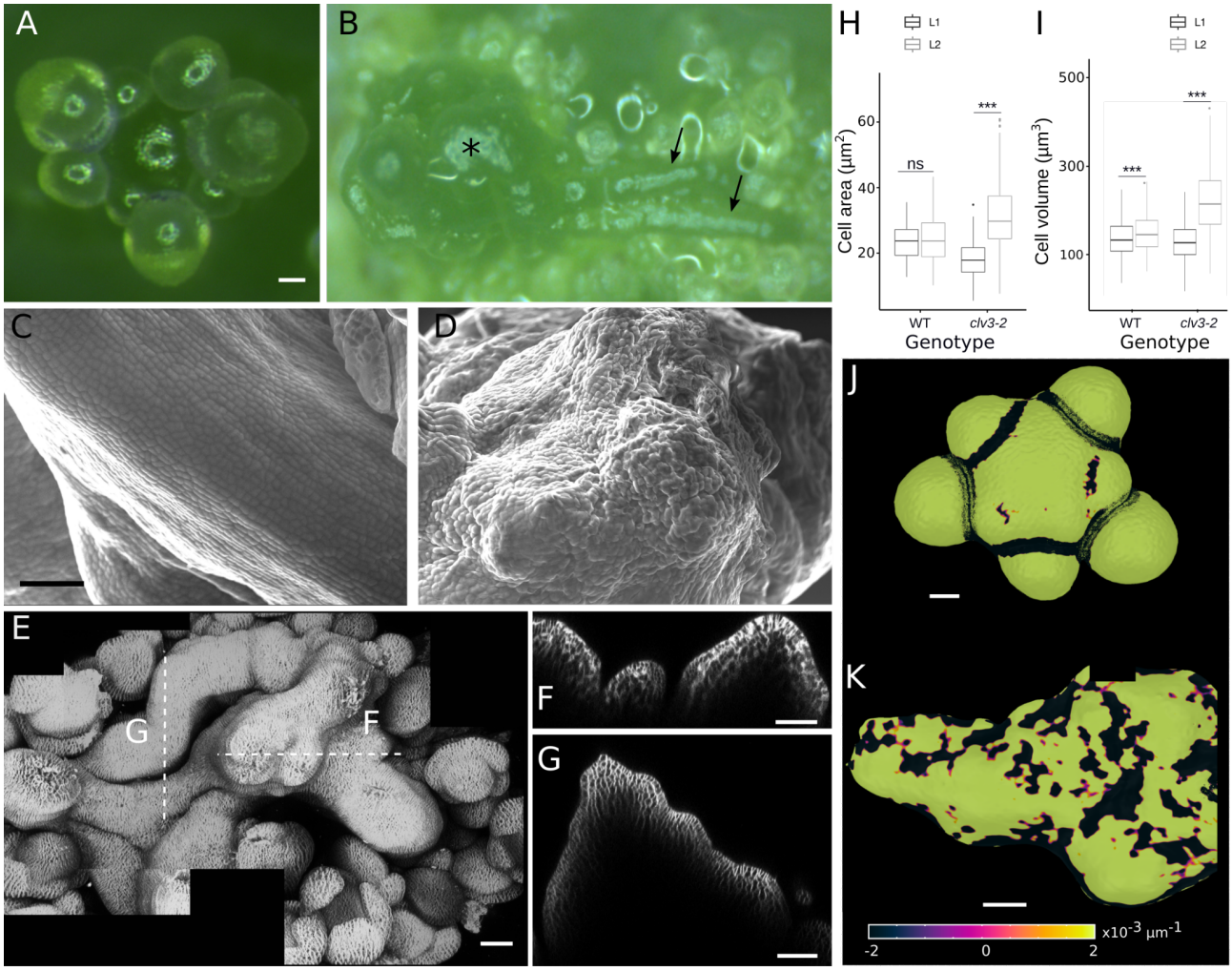

Figure 1. Altered cell and tissue properties characterise fasciated SAM

(A, B) Bright field images showing dissected WT (A) and *clv3-2* (B) SAM. The asterisk in (B) shows the central outgrowth and arrows point out two linear elongations. **(C, D)** SEM images showing cell organisation in the linear part of a *clv3-2* SAM (C), and at the top of an outgrowth (D). **(E-G)** Maximum intensity projection of a 3D confocal stack showing a *clv3-2* fasciated SAM. Cell membranes are stained with FM4-64. Dashed lines represent orthogonal sections shown in (F, G), through elongated areas and an outgrowth, respectively. **(H)** Boxplots of cell area in the L1 (black) and L2 (grey) cell layers of WT and *clv3-2* SAM. Mean ± s. d. areas are 23.9 ± 5.83 µm^2 for WT L1, 24.5 ± 7.18 µm^2 for WT L2, 18.4 ± 5.34 µm^2 for *clv3-2* L1, and 31.2 ± 9.84 µm^2 for *clv3-2* L2. L1 and L2 cells have significantly different areas in *clv3-2* mutants (Welch's t-test,, p = 4.65e-54) but not in WT plants (Welch's t-test, p = 0.545). n = 103 (L1) and 115 (L2) cells from 3 WT SAM, 400 (L1) and 244 (L2) cells from 3 *clv3-2* SAM. **(I)** Boxplots of cell volumes within the L1 (black) and the L2 (grey) cell layers of WT and *clv3-2* SAM. Outliers are not shown. Mean ± s. d. volumes are 136.51 ± 40.45 µm^3 for WT L1, 148.72 ± 44.54 µm^3 for WT L2, 129.48 ± 40.86 µm^3 for *clv3-2* L1, and 249.08 ± 130.65 µm^3 for *clv3-2* L2. L1 and L2 cells have significantly different volumes in WT (Welch's t-test, p = 2.32e-9)

and c*lv3-2* (Welch's t-test, p = 1.53e-204), but the general trend observed is that in *clv3-2*, cell volumes in the L2 are much greater than in the L1, whereas in the WT the two layers show similar cell volume values. n= 1468 L1 cells and 529 L2 cells from 4 WT SAM; 6426 L1 cells and 3428 L2 cells from 3 *clv3-2* SAM. Scale bars = 100 µm (A), 20 µm (B). **(J, K)** Colour maps quantifying the local curvature in a WT (J) and a *clv3-2* (K) SAM. Only a fragment of the mutant SAM is shown in (K) due to very large fasciation. Colour scale in μm^{-1}. Scale bars: 30 µm (A, B, shown in A), 25 µm (C, D, shown in C), 50 µm (E-G, K), 20 µm (J).

Figure 2

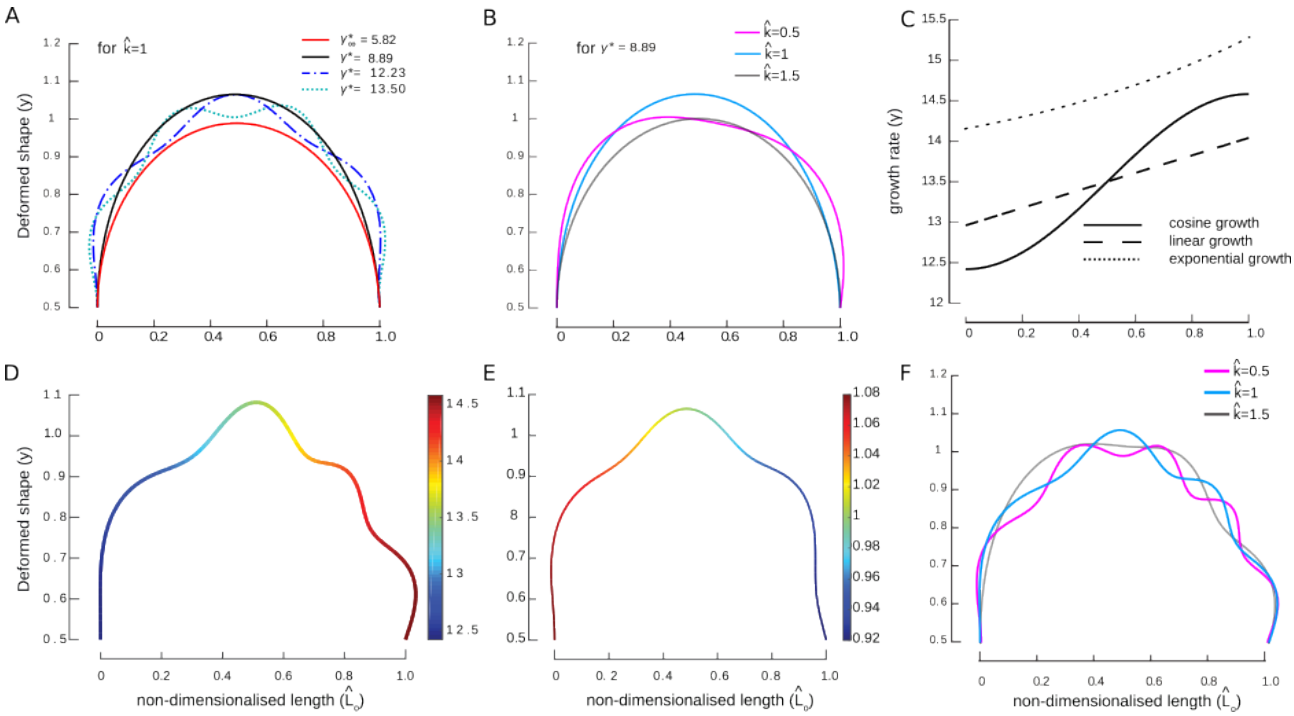

Figure 2. Growth and stiffness influence SAM shapes via growth-induced buckling

(A) Deformed shapes due to growth-induced buckling obtained for different values of critical growth rates (γ*) causing various buckling modes, with the stiffness of the underlying foundation fixed ($\hat{k}$=1). **(B)** Deformed shapes due to stiffness-induced buckling obtained for different values of foundation stiffness ($\hat{k}$=0.5, 1, 1.5), with the growth rate fixed (γ*=8.99). **(C)** The choice of growth law affects the deformed shapes. We select three different forms of growth laws for the same value of growth rate γ_0 - cosine, linear and exponential. **(D)** Deformed shape obtained as a result of growth-induced buckling in the case of cosine growth distribution. **(E)** Deformed shape obtained as a result of stiffness-induced buckling in the case of cosine stiffness distribution. **(F)** Effect of foundation stiffness on the asymmetric rod shapes obtained using growth heterogeneity.

Figure 3

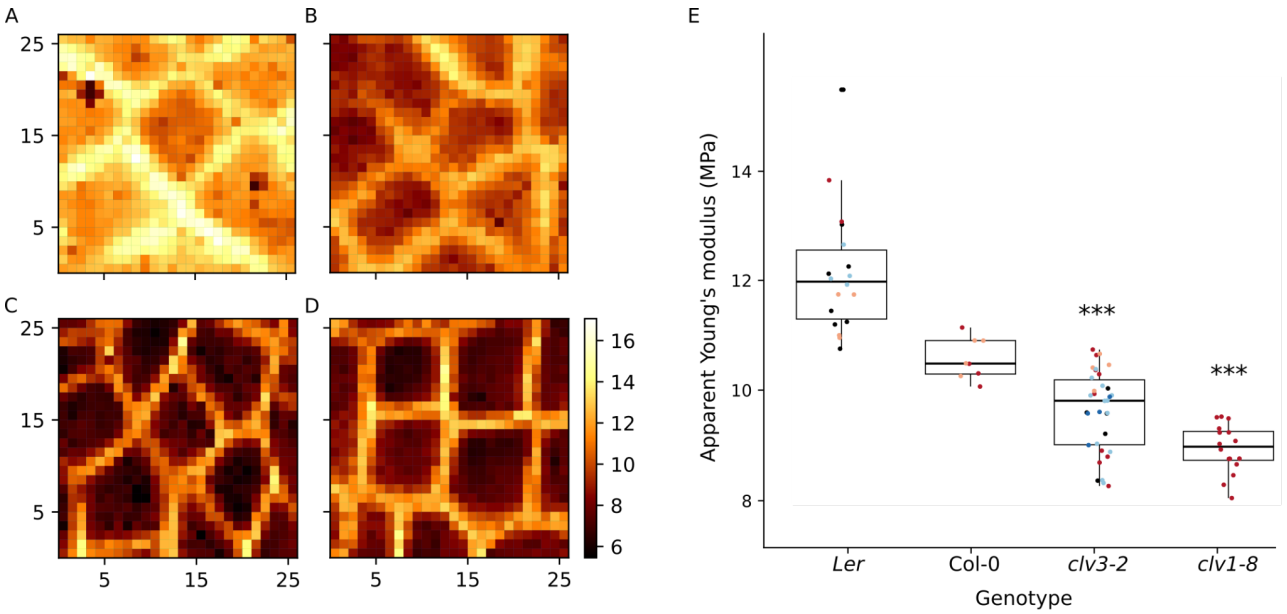

Figure 3. Loss of *clv* is associated with a reduction in epidermal cell stiffness

(A-D) Representative apparent Young's modulus maps of L*er* (A), Col-0 (B), *clv3-2* (C), and *clv1-8* (D) SAM. The colour scale quantifies the apparent Young's modulus (MPa). x, y axis: pixel number. **(E)** Box plots of mean apparent Young's moduli (MPa) measured on epidermal cells of L*er* (n=11), Col-0 (n=2), *clv3-2* (n=8), and *clv1-8* (n=1) SAM. Mean $\pm$ s. d. values are 12.16 $\pm$ 1.17 MPa for L*er*, 9.63 $\pm$ 0.74 MPa for *clv3-2*, 10.58 $\pm$ 0.38 MPa for Col-0, 8.94 $\pm$ 0.45 MPa *clv1-8*. On average, *clv3-2* and *clv1-8* have significantly lower apparent Young's moduli than the WT (L*er* for *clv3-2*, and Col-0 for *clv1-8*, respectively), as represented by *** (Welch's t-test, p=6.65e-8, p=1.85e-7 respectively). Black dots: each dot represents the mean apparent Young's modulus of a single sample; coloured dots: one colour represents a single sample for which several non-overlapping acquisitions were made, each dot shows the mean apparent Young's modulus per acquisition.

Figure 4

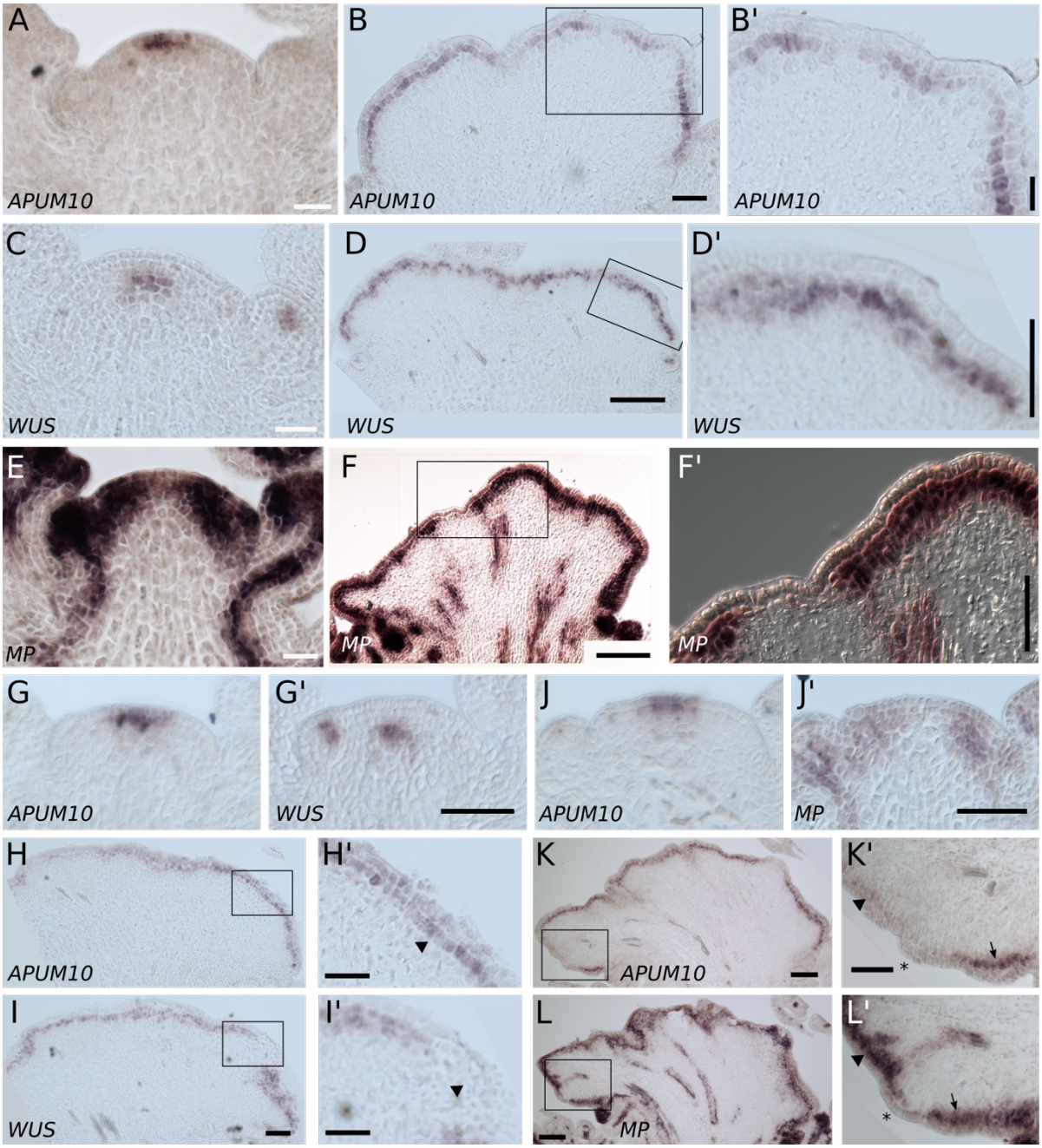

Figure 4. Gene expression is heterogenous in *clv3* SAM

(A-F') RNA *in situ* hybridisation of probes *APUM10* (A-B'), *WUS* (C-D'), and *MP* (E-F') on WT (A, C, E) and *clv3-2* (B, B', D, D', F, F') SAM. (B', D', and F') are close ups of the regions boxed in (B, D, and F), respectively. **(G-L')** *APUM10* (G, J, H, H', K, K'), *WUS* (G', I, I'), and *MP* (J', L, L') probes hybridised on consecutive sections of a single WT (G, G', J, J') or *clv3-2* (H-I', K-L') SAM. In (H',I'), arrowheads point to zones where *APUM10* mRNA is detected but not that of *WUS*. In (K', L'), arrowheads point to zones where *MP* mRNA is detected but not that of *APUM10*, asterisks show areas without *APUM10* nor *MP* probe detection, and arrows represent zones where both probes are detected. (H', I', K', and L') are close ups of the boxed areas shown in (H, I, K, and L), respectively. Section thickness: 10 µm. Scale bars: 50 µm (A, B', C, D', E, F', G, G', H', I', J, J', K', L'), 100 µm (B, D, F, H, I, K, L).

Figure 5

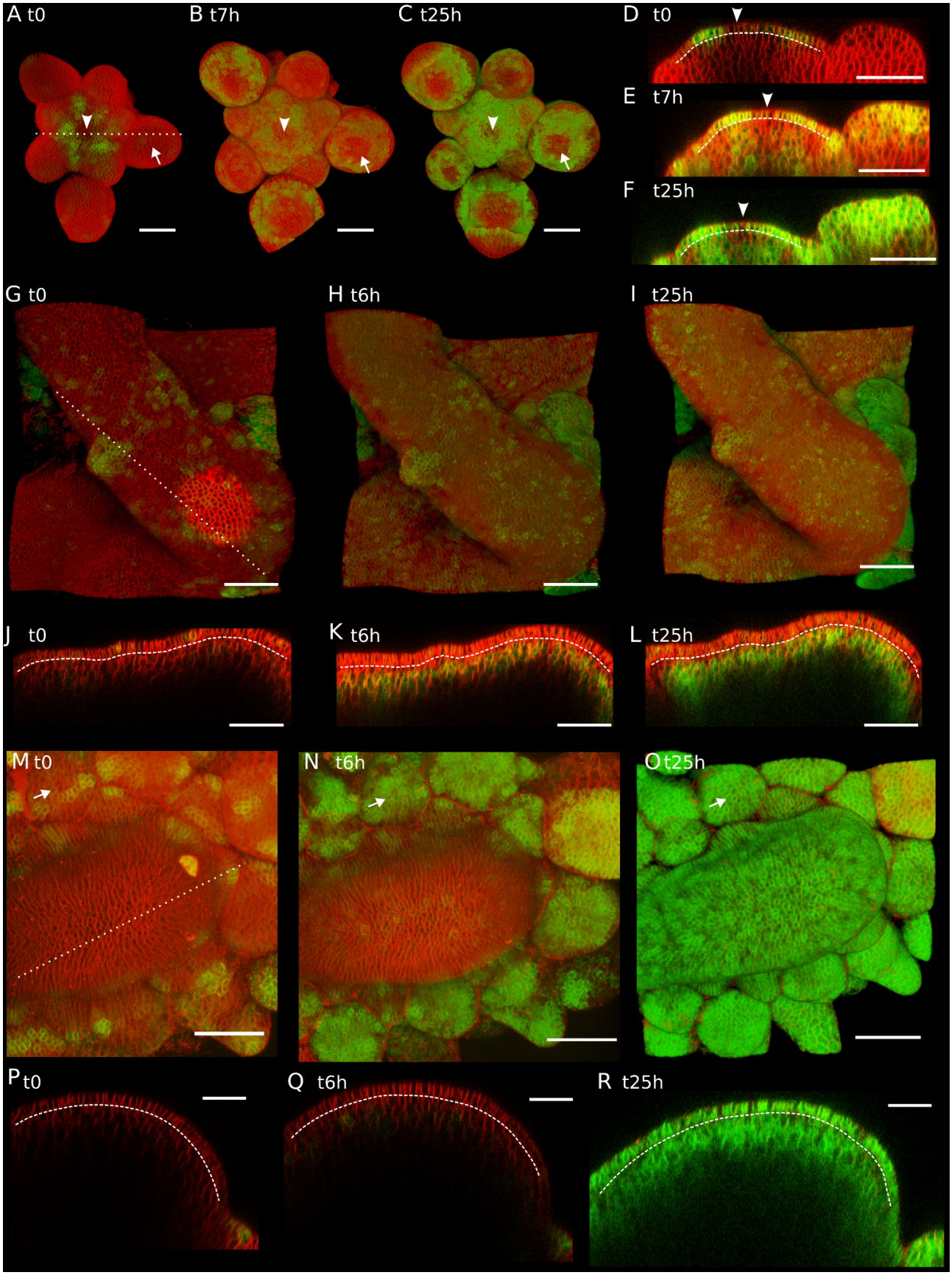
A t0
B t7h
C t25h
D t0
E t7h
F t25h
G t0
H t6h
I t25h
J t0
K t6h
L t25h
M t0
N t6h
O t25h
P t0
Q t6h
R t25h

Figure 5. *clv3* meristematic cells strongly respond to exogenous auxin

Projections of confocal stacks showing the effect of 1 mM IAA exogenous treatment on WT **(A-F)** and *clv3-2* **(G-R)** SAM expressing the *DR5::GFPer* reporter. The pictures show samples before treatment (A, D, G, J, M, P), 6 or 7 hours (B, E, H, K, N, Q), and 25 hours (C, F, I, L, O, R) after the 5-hour IAA treatment. (G-L) *clv3-2* SAM representative of the first group of responses to IAA (n=4/6). (M-R) *clv3-2* SAM representative of the second group of responses to IAA (n=2/6). Orthogonal views of the SAM in (D-F, J-L, P-R) are taken along the dotted lines shown in (A, G, M), respectively. Arrowheads in (A-F) indicate the centre of the SAM, arrows in (A-C, M-O) show representative flowers, and dashed lines in orthogonal sections represent the interface between L1 and L2 layers. Scale bars: 50 µm (A-O), 30 µm (P-R). n = 7 WT SAM, n = 6 *clv3-2* SAM. This experiment was replicated four times in the laboratory.

1